Sputtering-induced reemergence of the topological surface state in Bi_2Se_3

Raquel Queiroz,[1,*] Gabriel Landolt,[2,3] Stefan Muff,[3,4] Bartosz Slomski,[2,3] Thorsten Schmitt,[3] Vladimir N. Strocov,[3] Jianli Mi,[5] Bo Brummerstedt Iversen,[5] Philip Hofmann,[5] Jürg Osterwalder,[2] Andreas P. Schnyder,[1,†] and J. Hugo Dil[3,4,‡]

[1]*Max-Planck-Institut für Festkörperforschung, Heisenbergstrasse 1, D-70569 Stuttgart, Germany*

[2]*Physik-Institut, Universität Zürich, Winterthurerstrasse 190, CH-8057 Zürich, Switzerland*

[3]*Swiss Light Source, Paul Scherrer Institut, CH-5232 Villigen, Switzerland*

[4]*Institute of Physics, Ecole Polytechnique Fédérale de Lausanne, CH-1015 Lausanne, Switzerland*

[5]*Department of Physics and Astronomy, Interdisciplinary Nanoscience Center, Aarhus University, 8000 Aarhus C, Denmark*

(Received 18 December 2015; revised manuscript received 22 March 2016; published 8 April 2016)

We study the fate of the surface states of Bi_2Se_3 under disorder with strength larger than the bulk gap, caused by neon sputtering and nonmagnetic adsorbates. We find that neon sputtering introduces strong but dilute defects, which can be modeled by a unitary impurity distribution, whereas adsorbates, such as water vapor or carbon monoxide, are best described by Gaussian disorder. Remarkably, these two disorder types have a dramatically different effect on the surface states. Our soft x-ray angle-resolved photoemission spectroscopy (ARPES) measurements combined with numerical simulations show that unitary surface disorder pushes the Dirac state to inward quintuplet layers, burying it below an insulating surface layer. As a consequence, the surface spectral function becomes weaker but retains its quasiparticle peak. This is in contrast to Gaussian disorder, which smears out the quasiparticle peak completely. At the surface of Bi_2Se_3, neon sputtering adds additional unitary scatterers to the Gaussian disorder of the adsorbates. Since the introduced unitary disorder pushes the surface state to inward layers, the effects of Gaussian disorder are reduced. As a result the ARPES signal becomes sharper upon sputtering.

DOI: 10.1103/PhysRevB.93.165409

I. INTRODUCTION

An important hallmark of three-dimensional topological insulators are their protected Dirac-cone surface states, which connect bulk valence and conduction bands [1–3]. Since these surface states arise due to a nontrivial wave function topology in the bulk [4], they are robust to nonmagnetic disorder with strength γ smaller than the bulk gap Δ [5–11]. Moreover, their existence is independent of the surface orientation [12,13] and the local surface chemistry. Protected topological surface states have been experimentally observed in numerous topological insulators, such as $Bi_{1-x}Sb_x$ [14], Bi_2Se_3 [15], and Bi_2Te_3 [16], by both angle-resolved photoemission spectroscopy (ARPES) [17–22] and scanning tunneling experiments [23,24]. State-of-the-art spin-resolved ARPES has allowed to map out the predicted helical spin texture of the surface states [25–29]. However, in recent experiments only little attention has been given to the fundamental property that gave these materials their name, namely, the topological protection of the surface states against disorder [30,31].

The surface of Bi_2Se_3 and other Bi-based topological insulators adsorbs H_2O, H_2, or CO molecules upon exposure to air or vacuum rest gas [32–35]. This introduces a large number of impurity scatterers. Furthermore, as a result of chemical bonding between the adsorbates and the surface, the number of surface carriers is increased, which leads to band bending and the development of two-dimensional surface quantum well states [32,33]. Additional scattering centers on Bi_2Se_3 surfaces are caused by step edges and Se vacancies, which host impurity bound states with energies of the order or larger than the band gap [30,36]. While the adsorbates lead to a dense distribution of relatively weak impurities, the step edges and Se vacancies introduce a dilute distribution of very strong scatterers. The former is commonly called Gaussian disorder [37–40] and the latter is known as unitary disorder. Unitary scatterers can also be artificially created on the surface by sputtering it with neon or argon ions [36]. Due to their topological protection, the surface states are robust against both types of disorder as long as the disorder strength γ is smaller than the bulk gap Δ [5–8,39–41], but not necessarily otherwise.

In this article, we combine the first soft x-ray ARPES measurements of a topological surface state with numerical simulations to study how the surface states of Bi_2Se_3 are modified in the presence of strong disorder with $\gamma \gg \Delta$. We use UHV rest gas exposure to create Gaussian disorder and employ neon sputtering to introduce unitary disorder on the surface of Bi_2Se_3 (Fig. 1). Our numerical simulations show that the type of disorder matters for the topological insulator surface state. We find that Gaussian disorder with $\gamma \gg \Delta$ introduces a large number of impurity scatterers, which leads to a strong coupling between the bulk and surface states [41]. As a consequence, the momentum-space structure of the Dirac surface state is completely smeared out, leading to a surface spectral function that exhibits only broad features but no sharp quasiparticle peak (Fig. 2). Unitary disorder, on the other hand, creates a topologically trivial insulator at the surface, thereby pushing the Dirac state to inward quintuplet layers which are less disordered. Hence, unitary scatterers do not destroy the quasiparticle peak in the surface spectral function but only reduce its sharpness and intensity. Our ARPES measurements of Bi_2Se_3 surfaces show that the spectral function becomes sharper upon sputtering (Fig. 3). This seemingly paradoxical observation is explained by taking into account the different

*r.queiroz@fkf.mpg.de
†a.schnyder@fkf.mpg.de
‡hugo.dil@epfl.ch

 ©2016 American Physical Society

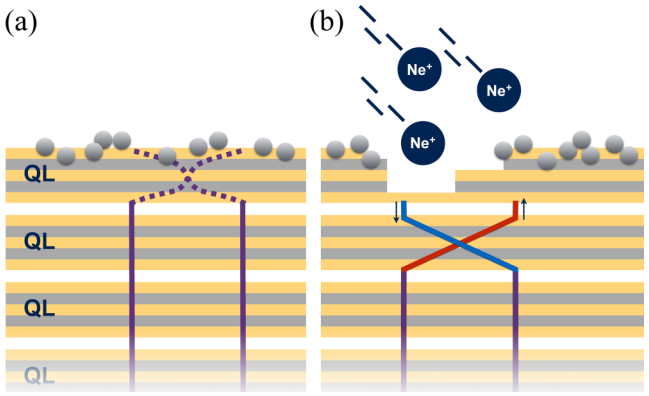

FIG. 1. Illustration of the reemergence of the topological surface state in Bi_2Se_3 upon sputtering. (a) Vacuum rest gas exposure leads to the absorption of water vapor and other molecules, giving rise to Gaussian surface disorder (gray circles). This results in a broadening and weakening of the ARPES spectral function. (b) Neon sputtering introduces vacancies and defects at the surface, thereby pushing the surface states to inward quintuplet layers (QL).

disorder types of the surface adsorbates and the sputtering-induced impurities. That is, neon sputtering reduces the effects of Gaussian disorder at the expense of introducing unitary scatterers. Since unitary disorder has a weaker effect on the spectral function than Gaussian disorder, the quasiparticle peaks in the ARPES signal become more pronounced due to sputtering.

II. NUMERICAL SIMULATIONS

To simulate the effects of disorder on the Bi_2Se_3 surface states, we employ a low-energy tight-binding Hamiltonian that describes the Bi-p_z and Se-p_z orbital bands close to the Γ point of the Brillouin zone [42]. The Hamiltonian can be conveniently expressed in terms of the spinor $\Phi_{\mathbf{k}} = (|p^1_{z,\mathbf{k}},\uparrow\rangle,|p^1_{z,\mathbf{k}},\downarrow\rangle,|p^2_{z,\mathbf{k}},\uparrow\rangle,|p^2_{z,\mathbf{k}},\downarrow\rangle)$ as $\mathcal{H} = \frac{1}{2}\sum_{\mathbf{k}} \Phi^\dagger_{\mathbf{k}} H_{\mathbf{k}} \Phi_{\mathbf{k}}$, with

$$H_{\mathbf{k}} = \epsilon_{\mathbf{k}}\sigma_0 \otimes \tau_0 + m_{\mathbf{k}}\sigma_0 \otimes \tau_3 + \sum_{i=0}^{2} a^i_{\mathbf{k}}\sigma_i \otimes \tau_1, \qquad (1)$$

where the two sets of Pauli matrices, σ_α and τ_α, describe the spin and orbital degrees of freedom, respectively. The tight-binding model $H_{\mathbf{k}}$ is defined on a rhombohedral lattice with lattice constants $a = 4.08$ Å and $c = 29.8$ Å. Equation (1) contains a kinetic term $\epsilon_{\mathbf{k}} = D_1[1-\cos(k_z c)] + D_2[3 - 2\cos(k_x\sqrt{3}a/2)\cos(k_y a/2) - \cos(k_y a)] - \mu$, a mass term $m_{\mathbf{k}} = B_1[1 - \cos(k_z c)] + B_2[3 - 2\cos(k_x\sqrt{3}a/2)\cos(k_y a/2) - \cos(k_y a)] + M$, and an interorbital coupling, which is parameterized by the vector $\mathbf{a}_{\mathbf{k}}$ with the three components $a^0_{\mathbf{k}} = A_0\sin(k_z c)$, $a^1_{\mathbf{k}} = A_1\sqrt{3}\sin(k_x\sqrt{3}a/2)\cos(k_y a/2)$, and $a^2_{\mathbf{k}} = A_1[\cos(k_x\sqrt{3}a/2)\sin(k_y a/2) + \sin(k_y a)]$. For the numerical calculations, the tight-binding parameters are determined by a fit of the energy spectrum of $H_{\mathbf{k}}$ to that of *ab initio* density functional theory (DFT) calculations [42–44]. We observe that Hamiltonian (1) satisfies time-reversal symmetry but, importantly, breaks sublattice (chiral) symmetry [11], which is in contrast to the model considered in Ref. [41].

We implement surface disorder due to adsorbates and lattice defects by adding the potential $\delta\mathcal{H}$ to the Hamiltonian (1), with

$$\delta\mathcal{H} = \sum_{\mathbf{k},\mathbf{q}_\parallel}\sum_{a=\mathrm{G,U}} \Phi^\dagger_{\mathbf{k}}\sigma_0 \otimes \left[V^{\mathrm{m}}_a(\mathbf{q}_\parallel)\tau_3 + V^{\mu}_a(\mathbf{q}_\parallel)\tau_0\right]\Phi_{\mathbf{k}+\mathbf{q}_\parallel}, \qquad (2)$$

where $V^b_a(\mathbf{q}_\parallel) = (1/\sqrt{\mathcal{N}})\sum_n v^b_a(\mathbf{r}_n)e^{-i\mathbf{q}_\parallel\cdot\mathbf{r}_n}$ represents the Fourier transform of the uncorrelated random onsite potentials

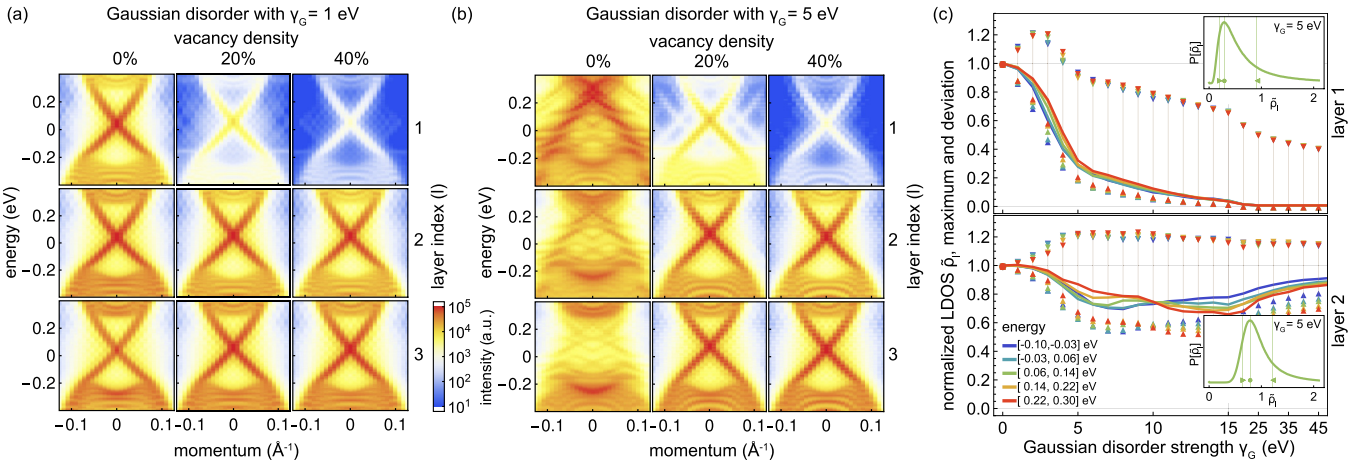

FIG. 2. (a, b) Layer resolved spectral function $A_l(\omega,\mathbf{k}_\parallel)$, Eq. (3), as a function of surface momentum $\mathbf{k}_\parallel$ along the $\overline{\mathrm{M}}$–$\overline{\Gamma}$–$\overline{\mathrm{M}}$ direction of the (001) surface Brillouin zone, obtained by diagonalizing tight-binding model (1). The magnitude of $A_l(\omega,\mathbf{k}_\parallel)$ is indicated by the logarithmic color scale, with blue and red representing low and high intensity, respectively. The same color scale is used for all subpanels. The effects of surface adsorbates is simulated by Gaussian disorder with (a) $\gamma_{\mathrm{G}} = 1$ eV and (b) $\gamma_{\mathrm{G}} = 5$ eV. To mimic the sputtering process, the density of surface defects is increased from $\gamma_{\mathrm{U}} = 0\%$ in the left columns to $\gamma_{\mathrm{U}} = 40\%$ in the right columns. (c) Energy-resolved distribution of the local density of states $P[\tilde{\rho}_l(\omega)]$ for the surface and the first inward quintuplet layer as a function of Gaussian disorder strength. The solid line represents the maximum of the distribution, whereas the triangles and inverted triangles indicate the left and right standard deviation, respectively, as defined in the Appendix. The insets show the probability distributions for the disorder strength $\gamma_{\mathrm{G}} = 5$ eV.

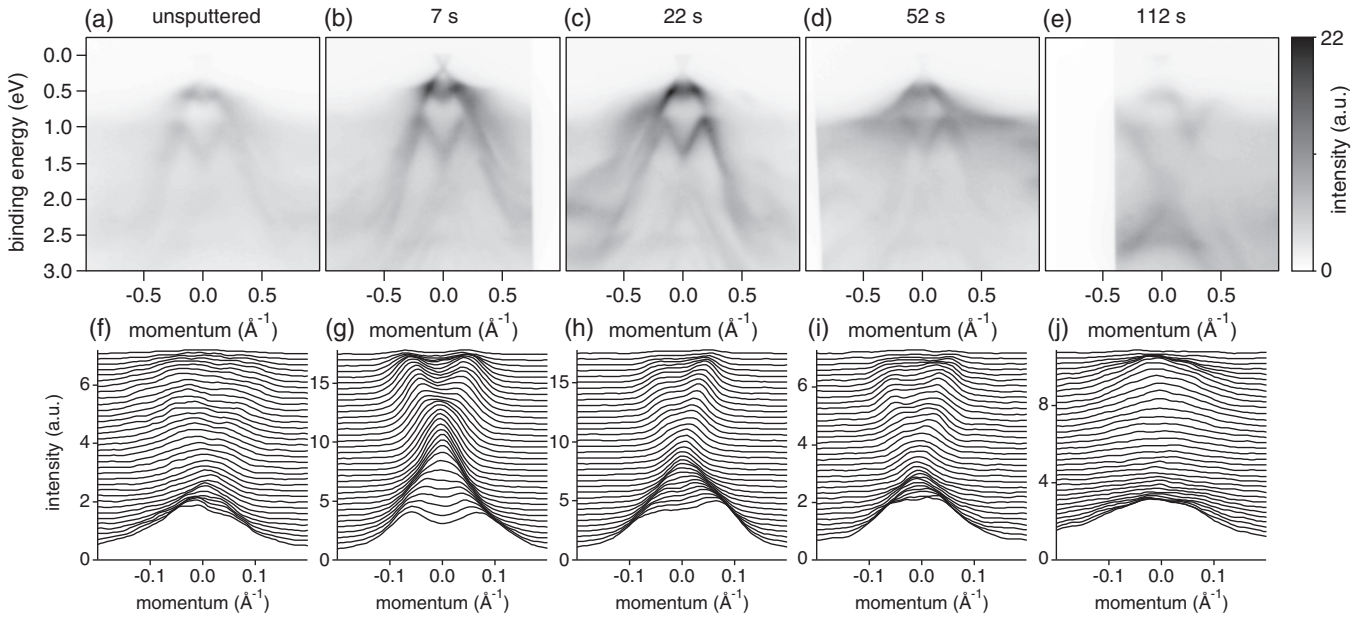

FIG. 3. Effects of neon sputtering on the (001) surface states of Bi_2Se_3. The upper row [panels (a)–(e)] shows SX-ARPES band maps with a photon energy of $h\nu = 380$ eV along the $\overline{\mathrm{M}}$–$\overline{\Gamma}$–$\overline{\mathrm{M}}$ crystallographic direction and as a function of neon sputtering. In all panels the same gray scale is used to indicate the ARPES intensity, with white and black corresponding to low and high signals, respectively. The lower row [panels (f)–(j)] displays the momentum distribution curves (MDCs) that correspond to the band maps of the upper row. Each curve is shifted vertically for clarity. The MDCs from the top to the bottom have binding energies from 0 meV up to 442 meV, with a spacing of 13 meV between traces.

$v_a^b(\mathbf{r}_n)$ at the surface sites $\mathbf{r}_n$. The disorder potential δH includes both local variations in the mass term ($b = \mathrm{m}$) and in the chemical potential ($b = \mu$). For the surface adsorbates we employ a Gaussian-type disorder distribution ($a = \mathrm{G}$), whereas for the lattice defects a unitary disorder distribution ($a = \mathrm{U}$) is used. To realize the latter, we randomly choose N_{imp} impurity sites $\mathbf{r}_i$ ($i = 1,2,\ldots,N_{\mathrm{imp}}$) at the surface, which all have the same large onsite potential $v_{\mathrm{U}}^b(\mathbf{r}_i) = 10^5$ eV. To implement the former, random potentials $v_{\mathrm{G}}^b(\mathbf{r}_n)$ at each lattice site $\mathbf{r}_n$ are drawn from a box distribution with width γ_{G} and $p[v_{\mathrm{G}}^b(\mathbf{r}_n)] = 1/\gamma_{\mathrm{G}}$ for $v_{\mathrm{G}}^b(\mathbf{r}_n) \in [-\gamma_{\mathrm{G}}/2, +\gamma_{\mathrm{G}}/2]$ [37]. Note that the strength of the Gaussian disorder is determined by the width γ_{G} of the distribution, while the strength of the unitary disorder is determined by the impurity density $\gamma_{\mathrm{U}} = N_{\mathrm{imp}}/N_{\mathrm{tot}}$, where N_{tot} is the total number of surface sites.

The effects of impurities on the Dirac surface state are best revealed by examining the momentum-resolved spectral function $A_l(\omega,\mathbf{k}_\parallel)$ [40,41], which is directly proportional to the ARPES intensity. The spectral function in the lth quintuplet layer is given by

$$A_l(\omega,\mathbf{k}_\parallel) = -\frac{\hbar}{4\pi}\mathrm{Im}\sum_{m,\nu}\frac{\left|\frac{1}{\sqrt{\mathcal{N}}}\sum_n \Psi_{\nu,l}^m(\mathbf{r}_n)e^{-i\mathbf{k}_\parallel\cdot\mathbf{r}_n}\right|^2}{\omega - E_m + i\eta}, \quad (3)$$

where ν is the band index and (E_m, $\Psi_{\nu,l}^m$) represents the eigensystem of the Hamiltonian (1) with surface disorder (2). Using exact diagonalization algorithms [45] we evaluate expression (3) for a (001) slab of dimension $100\times25\times25$ and an intrinsic broadening of $\eta = 0.02$ eV.

Figure 2 shows the spectral function for the first three outermost layers in the presence of unitary scatterers and Gaussian disorder with strength $\gamma_{\mathrm{G}} = 1$ eV in panel (a) and $\gamma_{\mathrm{G}} = 5$ eV in panel (b). We observe that Gaussian disorder with $\gamma_{\mathrm{G}} = 1$ eV, which is of the order of the bulk gap Δ, does not alter the surface states, apart from small broadening effects. That is, the Dirac-cone surface state is clearly visible as a sharp quasiparticle peak in $A_l(\omega,\mathbf{k}_\parallel)$, which decays exponentially into the bulk on the length scale of about three quintuplet layers [left column in Fig. 2(a)]. However, for Gaussian disorder with $\gamma_{\mathrm{G}} = 5$ eV, the momentum-space structure of the Dirac state is completely destroyed. This is due to a large number of impurity bound states at the surface, which leads to a strong coupling between bulk and surface states. Thus, $A_l(\omega,\mathbf{k}_\parallel)$ in the presence of very strong Gaussian disorder exhibits only broad humps but no sharp features [left column in Fig. 2(b)]. It is important to note that even though the disorder $\delta\mathcal{H}$ completely breaks translation symmetry along the surface, the $\mathbb{Z}_2$ topological invariant in the bulk remains well defined. As a consequence, there exists a band of delocalized subgap states at the boundary of the topological insulator $H_{\mathbf{k}}$, even for very strong surface disorder [7–11]. Since these delocalized states are not eigenstates of the surface momentum, they do not reveal themselves in Fig. 2(b). However, the distribution of the local density of states $P[\tilde{\rho}_l]$ for $\gamma_{\mathrm{G}} = 5$ eV indicates that there exist delocalized states both in the surface layer ($l = 1$) and the first inward quintuplet layer ($l = 2$) [Fig. 2(c)] (for details see Appendix). That is, $P[\tilde{\rho}_{l=2}]$ is peaked close to $\tilde{\rho}_l = 1$, while $P[\tilde{\rho}_{l=1}]$ exhibits a tail that extends beyond $\tilde{\rho}_l = 1$ [46]. In fact, our numerical data show that the surface state can never be completely localized. Even for arbitrarily strong Gaussian disorder, $P[\tilde{\rho}_{l=2}]$ has its maximum close to $\tilde{\rho}_l = 1$. We note that $P[\tilde{\rho}_l]$ is almost energy independent, which is in contrast to the sublattice symmetric model of Ref. [41], where $\omega = 0$ is distinct from other energies.

To simulate the sputtering process, we increase the density of surface defects from $\gamma_{\mathrm{U}} = 0\%$ to $\gamma_{\mathrm{U}} = 40\%$. The right

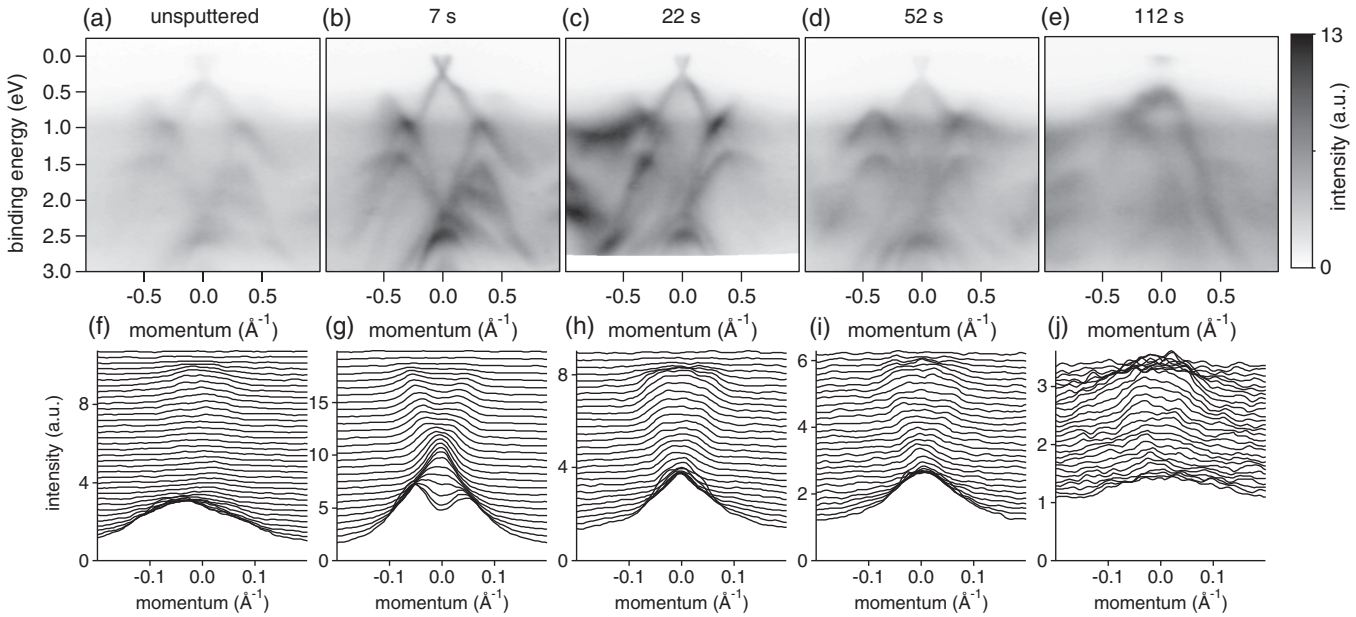

FIG. 4. SX-ARPES measurements of the (001) Bi_2Se_3 surface with a photon energy of $h\nu = 725$ eV. The upper row [panels (a)–(e)] shows the band maps along the $\overline{M}$–$\overline{\Gamma}$–$\overline{M}$ crystallographic direction for different sputtering times. The ARPES intensity is indicated by the gray scale, with black and white corresponding to high and low intensity, respectively. The lower row [panels (f)–(j)] displays the momentum distribution curves (MDCs) for binding energies ranging from 0 meV to 442 meV with a spacing of 13 meV. For clarity each MDC is shifted vertically.

columns of Figs. 2(a) and 2(b) show that for $\gamma_U = 40\%$ the Dirac state is pushed to the second and third inward quintuplet layers, since the surface layer ($l = 1$) becomes more and more insulating. As a result the Dirac state reappears in the spectral function of the second and third layers as well-defined quasiparticle peaks.

III. SX-ARPES MEASUREMENTS

In order to measure the effects of sputtering on the Dirac surface state using ARPES, it is necessary to employ large incident photon energies, such that the probing depth is considerably larger than one Bi_2Se_3 unit cell. Therefore, instead of conventional UV-ARPES, we used soft x-ray (SX) ARPES with a probing depth, defined as 3 mean free path lengths, of about 30 Å [47,48], which corresponds to three Bi_2Se_3 quintuplet layers. The photoemission experiments were performed on *in situ* cleaved single crystals of Bi_2Se_3 at the ADRESS beamline of the Swiss Light Source using photon energies of $h\nu = 380$ eV and $h\nu = 725$ eV. To prevent freezing of the sputtering agent, the samples were cleaved and sputtered at room temperature. The SX-ARPES measurement, however, was carried out at the low temperature of 10 K, since otherwise the photoemission signal would be too blurry due to the loss of spectral coherence as expressed by the large Debye-Waller factor [49,50].

Our aim was to investigate how the surface spectral function is changed as the density of unitary scatterers is increased, while the Gaussian disorder of the surface adsorbates is kept constant. For that purpose, it was crucial to keep the times between cleaving, sputtering, cooling, and measuring the crystals fixed such that all samples were exposed for the same duration to the UHV rest gas at a base pressure better than 5×10^{-10} mbar after sputtering. The time between cooling down the sample and measuring was of the order of half an hour, resulting in the adsorption of a significant amount of H_2, CO, and H_2O molecules. Different densities of unitary disorder were introduced by irradiating the Bi_2Se_3 surface for different time periods with Ne^+ ions with an energy of 0.7 keV at a pressure of 3×10^{-6} mbar. For every sputtering cycle a new sample was cleaved under identical circumstances. After sputtering, the sample was immediately *in situ* transferred to the measurement chamber to start the SX-ARPES experiment. To assure the reproducibility of the results, the sample surface was scanned for homogeneity and the measurements, especially for the unsputtered and lightly sputtered samples, were repeated several times. All data shown here were obtained under identical conditions with respect to beamline and analyzer settings, and integration time.

In Fig. 3 we present the SX-ARPES band maps and momentum distribution curves (MDCs) as a function of surface momentum along the $\overline{M}$–$\overline{\Gamma}$–$\overline{M}$ direction of the (001) surface Brillouin zone. The soft x-ray photon energy was taken to be $h\nu = 380$ eV and the sputtering time was increased from 0 s in panel (a) to 112 s in panel (e). In Fig. 4 we show the same maps obtained with a photon energy of $h\nu = 725$ eV. SX-ARPES is sensitive to different regions of the Brillouin zone at different energies, leading to distinctively different bulk bands in Figs. 3 and 4. On the other hand, the photoemission spectrum of the surface state does not depend on photon energy due to the lack of a k_z dependence in its energy dispersion. The surface state probed at this higher photon energy shows a qualitatively similar response to surface sputtering as in Fig. 3, with the only difference of having a higher intensity.

IV. DISCUSSION

We start by discussing the spectra of the unsputtered sample, Figs. 3(a) and 3(f). In the band map of Fig. 3(a) the bulk valence bands of the Bi-p and Se-p orbitals are clearly visible at $\sim$0.5 eV and $\sim$1.2 eV, respectively. Near the $\bar{\Gamma}$ point these valence bands exhibit a characteristic "M-shape" dispersion, which agrees with *ab initio* DFT calculations [21,42]. The Dirac surface state, however, is barely detectable, neither at $h\nu = 380$ eV nor at $h\nu = 725$ eV. This is due to the large amount of surface disorder introduced by the adsorbates, which smears out the quasiparticle peak of the Dirac state. Indeed, we find that the ARPES band map of Fig. 3(a) is in good agreement with the simulated spectral function of the Bi_2Se_3 surface in the presence of strong Gaussian disorder [left column of Fig. 2(b)]. We note that the photon energies are chosen such to select a k_z where the bulk conduction band is not observed. To the best of our knowledge, this constitutes the first measurement of the surface state of a topological insulator at such high photon energies.

Sputtering the surface for a few seconds reduces Gaussian disorder by removing adsorbates, but creates local defects, which increases unitary disorder. As a net effect, we find that the quasiparticle peaks in the spectral function of the bulk and surface bands become considerably sharper [Figs. 3(b) and 3(g)]. The "V-shaped" dispersion and the Dirac point of the surface state, which is located at $\sim$0.3 eV, are now clearly discernible. This observation corresponds well with the calculated spectral function of the middle column of Fig. 2(b), where the sputtering process was simulated by adding 20% surface vacancies.

For longer sputtering times the concentration of surface defects is further increased, but the Dirac surface state remains visible, albeit with a broader quasiparticle peak [Figs. 3(c) and 3(d)]. This observation can be explained by noting that a large density of defects eventually leads to an insulating surface layer, thereby pushing the Dirac surface state to the second and third inward unit cells. Since SX-ARPES is less sensitive to the second and third unit cells, the spectral function intensity of the Dirac state becomes weaker. This interpretation is confirmed by our numerical simulations of Fig. 2, which show that for 40% defect density most of the spectral weight of the Dirac state is concentrated in the second and third quintuplet layers. Moreover, this explanation is consistent with the fact that the Dirac surface state of sputtered Bi_2Se_3 is only visible in SX-ARPES but not in UV-ARPES [36], which has a smaller probing depth.

Finally, we find that sputtering for more than one minute radically changes the topography of the Bi_2Se_3 surface. That is, the entire crystal surface is cracked up into multiple tilted domains with sizes comparable to the synchrotron beam spot ($74\times30\,\mu$m). As a result, the ARPES spectra contain contributions from several domains with relative shifts in surface momenta, since the normal photoemission angle now sensitively depends on the incident position of the synchrotron light [Fig. 3(e)]. While a broad signature of the bulk bands can still be observed, the Dirac surface state is completely absent in the spectra of the strongly sputtered samples. This indicates that the surface of Bi_2Se_3 has been rendered topologically trivial up to a depth of more than three unit cells, i.e., beyond the probing depth of SX-ARPES.

V. CONCLUSION

In conclusion, we have investigating how topological insulator surface states are affected by disorder caused by neon sputtering and surface adsorbates. By comparing numerical simulations to SX-ARPES measurements of Bi_2Se_3, we have shown that the surface adsorbates correspond to Gaussian disorder, while the local defects introduced by sputtering represent unitary scatterers. We have demonstrated that the effects of Gaussian disorder can be reduced by sputtering, which introduces defects and vacancies in the surface layer. Since the latter push the surface state to inward layers, the effects of Gaussian disorder are reduced. As a consequence, the ARPES signal of Bi_2Se_3 surfaces that have been exposed to air (or UHV rest gas) become sharper upon sputtering. Our findings demonstrate the extreme robustness of the Bi_2Se_3 surface state against any type of surface disorder, thereby confirming its topological origin.

ACKNOWLEDGMENTS

This work was supported by the Swiss National Science Foundation under Project No. PP00P2_144742 1. A.P.S. was supported in part by the US National Science Foundation under Grant No. NSF PHY11-25915. P.H., J.L.M., and B.B.I. acknowledge support by the Villum Foundation, the DFG under Project SPPI666, and the Danish National Research Foundation.

APPENDIX: DISTRIBUTION OF LOCAL DENSITY OF STATES

Information about the localization or delocalization properties of the Dirac surface state can be obtained by computing the distribution of the local density of states (LDOS) $P[\tilde{\rho}_l(\omega)]$ [46]. The probability distribution $P[\tilde{\rho}_l(\omega)]$ is defined in terms of the normalized LDOS on the lth quintuplet layer

$$\tilde{\rho}_l(\omega) = \tilde{\rho}_l(\omega)/\langle\tilde{\rho}_l(\omega)\rangle, \tag{A1}$$

where $\langle\tilde{\rho}_l(\omega)\rangle$ denotes the mean value of the LDOS. The distributions shown in Fig. 2(c) in the main text have been computed for an ensemble of 1000 disordered Hamiltonians with 25^3 lattice sites in real-space and periodic boundary conditions along the x and y directions.

We note that a distribution $P[\tilde{\rho}_l(\omega)]$ centered at $\tilde{\rho}_l(\omega) = 1$ indicates that the majority of states are delocalized, while a distribution peaked at $\tilde{\rho}_l(\omega) = 1$ signals that most of the states are localized. The left (right) tails of the distribution give us insight as to whether there exists a minority of localized (delocalized) states. To quantify the size of these tails, we introduce the left and right standard deviations, σ_L and σ_R, of $P[\tilde{\rho}_l]$, which are given by

$$\sigma_L^2 = \mathcal{N}_L \sum_{\tilde{\rho}_l=0}^{\rho_{\max}} 2P[\tilde{\rho}_l](\tilde{\rho}_l - \rho_{\max})^2, \tag{A2}$$

$$\sigma_R^2 = \mathcal{N}_R \sum_{\tilde{\rho}_l=\rho_{\max}}^{\infty} 2P[\tilde{\rho}_l](\tilde{\rho}_l - \rho_{\max})^2. \tag{A3}$$

In the above definitions we have treated $\tilde{\rho}_l > \rho_{\max}$ and $\tilde{\rho}_l < \rho_{\max}$ as independent distributions, where $\rho_{\max}$ is the maximum or the distribution $P[\tilde{\rho}_l]$. $\mathcal{N}_{L,R}$ are the appropriate normalization constants.

[1] X.-L. Qi and S.-C. Zhang, Rev. Mod. Phys. **83**, 1057 (2011).
[2] M. Z. Hasan and C. L. Kane, Rev. Mod. Phys. **82**, 3045 (2010).
[3] C.-K. Chiu, J. C. Y. Teo, A. P. Schnyder, and S. Ryu, arXiv:1505.03535.
[4] C. L. Kane and E. J. Mele, Phys. Rev. Lett. **95**, 146802 (2005).
[5] K. Nomura, M. Koshino, and S. Ryu, Phys. Rev. Lett. **99**, 146806 (2007).
[6] S. Ryu, C. Mudry, H. Obuse, and A. Furusaki, Phys. Rev. Lett. **99**, 116601 (2007).
[7] P. M. Ostrovsky, I. V. Gornyi, and A. D. Mirlin, Phys. Rev. Lett. **98**, 256801 (2007).
[8] S. Ryu, A. P. Schnyder, A. Furusaki, and A. W. W. Ludwig, New J. Phys. **12**, 065010 (2010).
[9] A. P. Schnyder, S. Ryu, A. Furusaki, and A. W. W. Ludwig, Phys. Rev. B **78**, 195125 (2008).
[10] K. W. Kim, R. S. K. Mong, M. Franz, and G. Refael, Phys. Rev. B **92**, 075110 (2015).
[11] A. M. Essin and V. Gurarie, J. Phys. A: Math. Theor. **48**, 11FT01 (2015).
[12] C.-Y. Moon, J. Han, H. Lee, and H. J. Choi, Phys. Rev. B **84**, 195425 (2011).
[13] J. C. Y. Teo, L. Fu, and C. L. Kane, Phys. Rev. B **78**, 045426 (2008).
[14] D. Hsieh, D. Qian, L. Wray, Y. Xia, Y. S. Hor, R. J. Cava, and M. Z. Hasan, Nature (London) **452**, 970 (2008).
[15] D. Hsieh, Y. Xia, D. Qian, L. Wray, J. H. Dil, F. Meier, J. Osterwalder, L. Patthey, J. G. Checkelsky, N. P. Ong *et al.*, Nature (London) **460**, 1101 (2009).
[16] D. Hsieh, Y. Xia, D. Qian, L. Wray, F. Meier, J. H. Dil, J. Osterwalder, L. Patthey, A. V. Fedorov, H. Lin *et al.*, Phys. Rev. Lett. **103**, 146401 (2009).
[17] Y. L. Chen, J. G. Analytis, J.-H. Chu, Z. K. Liu, S.-K. Mo, X. L. Qi, H. J. Zhang, D. H. Lu, X. Dai, Z. Fang *et al.*, Science **325**, 178 (2009).
[18] Y. Xia, D. Qian, D. Hsieh, L. Wray, A. Pal, H. Lin, A. Bansil, D. Grauer, Y. S. Hor, R. J. Cava *et al.*, Nat. Phys. **5**, 398 (2009).
[19] S. Souma, K. Kosaka, T. Sato, M. Komatsu, A. Takayama, T. Takahashi, M. Kriener, K. Segawa, and Y. Ando, Phys. Rev. Lett. **106**, 216803 (2011).
[20] T. Sato, K. Segawa, K. Kosaka, S. Souma, K. Nakayama, K. Eto, T. Minami, Y. Ando, and T. Takahashi, Nat. Phys. **7**, 840 (2011).
[21] H. M. Benia, A. Yaresko, A. P. Schnyder, J. Henk, C. T. Lin, K. Kern, and C. R. Ast, Phys. Rev. B **88**, 081103 (2013).
[22] M. S. Bahramy, P. D. C. King, A. de la Torre, J. Chang, M. Shi, L. Patthey, G. Balakrishnan, P. Hofmann, R. Arita, N. Nagaosa *et al.*, Nat. Commun. **3**, 1159 (2012).
[23] P. Roushan, J. Seo, C. V. Parker, Y. S. Hor, D. Hsieh, D. Qian, A. Richardella, M. Z. Hasan, R. J. Cava, and A. Yazdani, Nature (London) **460**, 1106 (2009).
[24] J. Seo, P. Roushan, H. Beidenkopf, Y. S. Hor, R. J. Cava, and A. Yazdani, Nature (London) **466**, 343 (2010).
[25] D. Hsieh, Y. Xia, L. Wray, D. Qian, A. Pal, J. H. Dil, J. Osterwalder, F. Meier, G. Bihlmayer, C. L. Kane *et al.*, Science **323**, 919 (2009).
[26] S.-Y. Xu, Y. Xia, L. A. Wray, S. Jia, F. Meier, J. H. Dil, J. Osterwalder, B. Slomski, A. Bansil, H. Lin *et al.*, Science **332**, 560 (2011).
[27] S.-Y. Xu, M. Neupane, C. Liu, D. Zhang, A. Richardella, L. Andrew Wray, N. Alidoust, M. Leandersson, T. Balasubramanian, J. Sánchez-Barriga *et al.*, Nat. Phys. **8**, 616 (2012).
[28] S. V. Eremeev, G. Landolt, T. V. Menshchikova, B. Slomski, Y. M. Koroteev, Z. S. Aliev, M. B. Babanly, J. Henk, A. Ernst, L. Patthey *et al.*, Nat. Commun. **3**, 635 (2012).
[29] L. Fu, Phys. Rev. Lett. **103**, 266801 (2009).
[30] Z. Alpichshev, R. R. Biswas, A. V. Balatsky, J. G. Analytis, J.-H. Chu, I. R. Fisher, and A. Kapitulnik, Phys. Rev. Lett. **108**, 206402 (2012).
[31] F. Pielmeier, G. Landolt, B. Slomski, S. Muff, J. Berwanger, A. Eich, A. A. Khajetoorians, J. Wiebe, Z. S. Aliev, M. B. Babanly *et al.*, New J. Phys. **17**, 023067 (2015).
[32] M. Bianchi, D. Guan, S. Bao, J. Mi, B. B. Iversen, P. D. C. King, and P. Hofmann, Nat. Commun. **1**, 128 (2010).
[33] M. Bianchi, R. C. Hatch, J. Mi, B. B. Iversen, and P. Hofmann, Phys. Rev. Lett. **107**, 086802 (2011).
[34] H. M. Benia, C. Lin, K. Kern, and C. R. Ast, Phys. Rev. Lett. **107**, 177602 (2011).
[35] M. P. Stehno, V. Orlyanchik, C. D. Nugroho, P. Ghaemi, M. Brahlek, N. Koirala, S. Oh, and D. J. Van Harlingen, Phys. Rev. B **93**, 035307 (2016).
[36] R. C. Hatch, M. Bianchi, D. Guan, S. Bao, J. Mi, B. B. Iversen, L. Nilsson, L. Hornekær, and P. Hofmann, Phys. Rev. B **83**, 241303 (2011).
[37] W. A. Atkinson, P. J. Hirschfeld, A. H. MacDonald, and K. Ziegler, Phys. Rev. Lett. **85**, 3926 (2000).
[38] C. Chamon and C. Mudry, Phys. Rev. B **63**, 100503 (2001).
[39] R. Queiroz and A. P. Schnyder, Phys. Rev. B **89**, 054501 (2014).
[40] R. Queiroz and A. P. Schnyder, Phys. Rev. B **91**, 014202 (2015).
[41] G. Schubert, H. Fehske, L. Fritz, and M. Vojta, Phys. Rev. B **85**, 201105 (2012).
[42] H. Zhang, C.-X. Liu, X.-L. Qi, X. Dai, Z. Fang, and S.-C. Zhang, Nat. Phys. **5**, 438 (2009).
[43] S. Sasaki, M. Kriener, K. Segawa, K. Yada, Y. Tanaka, M. Sato, and Y. Ando, Phys. Rev. Lett. **107**, 217001 (2011).
[44] In our numerical calculation we set $A_1 = 0.540\,\text{eV}$, $A_2 = 0.673\,\text{eV}$, $B_1 = 0.301\,\text{eV}$, $B_2 = 4.55\,\text{eV}$, $D_1 = 0.0391\,\text{eV}$, $D_2 = 1.57\,\text{eV}$, $M = 0.28\,\text{eV}$, and $\mu = -0.0068\,\text{eV}$.
[45] R. B. Lehoucq, D. C. Sorensen, and C. Yang, *ARPACK Users' Guide: Solution of Large-Scale Eigenvalue Problems with Implicitly Restarted Arnoldi Methods* (Society for Industrial and Applied Mathematics, Philadelphia, PA, 1997).
[46] G. Schubert, J. Schleede, K. Byczuk, H. Fehske, and D. Vollhardt, Phys. Rev. B **81**, 155106 (2010).

[47] V. N. Strocov, T. Schmitt, U. Flechsig, T. Schmidt, A. Imhof, Q. Chen, J. Raabe, R. Betemps, D. Zimoch, J. Krempasky *et al.*, J. Synchrotron Radiat. **17**, 631 (2010).

[48] C. Powell, A. Jablonski, I. Tilinin, S. Tanuma, and D. Penn, J. Electron Spectrosc. Relat. Phenom. **98-99**, 1 (1999).

[49] P. Hofmann, C. Søndergaard, S. Agergaard, S. V. Hoffmann, J. E. Gayone, G. Zampieri, S. Lizzit, and A. Baraldi, Phys. Rev. B **66**, 245422 (2002).

[50] J. Braun, J. Minár, S. Mankovsky, V. N. Strocov, N. B. Brookes, L. Plucinski, C. M. Schneider, C. S. Fadley, and H. Ebert, Phys. Rev. B **88**, 205409 (2013).